Identification of the odd and even modes in Görtler flows subjected to a pressure gradient

Josuel K Rogenski, josuelkr@gmail.com
Leandro F de Souza, lefraso@icmc.usp.br
Instituto de Ciências Matemáticas e de Computação. Universidade de São Paulo.

Abstract. *Transition to turbulence in boundary layers flows over concave surfaces may occur due to the interaction between Görtler vortices and other unsteady disturbances. In the nonlinear regime both the sinuous and varicose modes are unstable modes and they lead the neutral Görtler flow to turbulence. The role of a external pressure gradient in the growth of secondary modes is numerically investigated. We confirm both secondary modes are potentially unstable even in the presence of a external pressure gradient different from zero. The sinuous mode is provided to be the most unstable mode for the cases under consideration.*

Keywords: *even and odd modes, secondary instability, Görtler vortices, high-order numerical simulation*

1. INTRODUCTION

The weakly nature of the centrifugal instability in boundary layer flows over slightly concave surfaces justifies the role of the secondary instability in the transition of a laminar flow to a turbulent state. In a region near saturation of Görtler vortices, nonlinear effects are responsible for high distortions in the mean flow profile. These distortions are experimentally visualized as the classical mushroom structure. This mushroom shape possesses inflectional points in the streamwise velocity component that are potentially unstable to unsteady disturbances.

Experimental evidence of the secondary instability role in the transition of a Görtler flow is provided by Swearingen and Blackwelder [1987]. The authors state the varicose and sinuous secondary modes are associated with high velocity gradients in the normal to the wall and spanwise directions, respectively [Saric, 1994]. Following Swearingen and Blackwelder [1987], many theoretical and experimental studies have been focused on the secondary instability field as in Hall and Horseman [1991], Li and Malik [1995] and Schrader et al. [2011]. Hall and Horseman [1991] supports the importance given to the experimentally observed harmonic modes and Li and Malik [1995] identify contributions from subhamonics modes in the transition. Li and Malik [1995] also confirms the existence of a relation between the characteristic wavelength and the selection of the dominant mode. The sinuous and subharmonic modes tend to be more unstable than the varicose mode in cases where the wavelength of the vortices is small.

Recently, experimental visualizations of Görtler vortices are provided by Winoto et al. [2005], Mitsudharmadi et al. [2005], Mitsudharmadi et al. [2006], Tandiono et al. [2009b] and Tandiono et al. [2009a]. Winoto et al. [2005] reports success in generating Gortler vortices by wavelengh imposition and in visualizing the growth of the secondary instability modes. At the same year, the authors discusses nonlinear effects in the process that leave vortices to split and merge. Mitsudharmadi et al. [2006] reaffirms vortices with characteristic wavenumber parameter equals to 250 as the most unstable ones. Tandiono et al. [2009b] highlights the secondary instability as the responsible to the observable increasing on shear stress values in comparison with data obtained in turbulent regimes.

Studies related to the pressure gradient influence on the secondary instability are only discussed based on experimental evidence and they are reported by Aihara and Sonoda [1981] and Bahri et al. [1999]. Based on this fact, mechanisms of the secondary instability on the transition of a Görtler flow are here investigated by the use of high-order numerical simulations. The aim of the present study is to confirm both the sinuous and varicose modes as potentially unstable in a Görtler flow subjected to a external constant pressure gradient.

2. PROBLEM FORMULATION

Stability analyses are done considering a mean-flow state represented by a two-dimensional boundary layer flow over a slightly concave surface. Assuming a flow quantity $\widetilde{g}$ represented by

$$\widetilde{g} = g_b + g, \tag{1}$$

where g_b is the mean-flow state, the following dimensionless transport equations in the streamwise (x), wall-normal (y) and spanwise (z) directions can be used to represent the disturbances of the flow [Souza et al., 2004, Malatesta et al., 2013]:

$$\frac{\partial \omega_x}{\partial t} + \frac{\partial a}{\partial y} - \frac{\partial b}{\partial z} + \frac{Go^2}{Re}\frac{\partial d}{\partial z} = \nabla^2 \omega_x, \tag{2}$$

$$\frac{\partial \omega_y}{\partial t} + \frac{\partial c}{\partial z} - \frac{\partial a}{\partial x} = \nabla^2 \omega_y, \tag{3}$$

$$\frac{\partial \omega_z}{\partial t} + \frac{\partial b}{\partial x} - \frac{\partial c}{\partial y} - \frac{Go^2}{Re}\frac{\partial d}{\partial x} = \nabla^2 \omega_z. \tag{4}$$

The ω_x, ω_y and ω_z are the components of the vorticity vector. We define vorticity as the opposite of the velocity vector $(u, v, w)^t$. Variable t is the time and $\nabla^2 = \left(\frac{1}{Re}\frac{\partial^2}{\partial x^2} + \frac{\partial^2}{\partial y^2} + \frac{1}{Re}\frac{\partial^2}{\partial z^2}\right)$. Re and Go are the Reynolds and Görtler numbers, respectively. Identifying dimensional quantities by an asterisk and assuming U^*_∞ is the potential streamwise velocity at an L^* position from the leading edge, nondimensionalization relations hold for

$$x = \frac{x^*}{L^*},\ y = \frac{1}{\sqrt{Re}}\frac{y^*}{L^*},\ z = \frac{z^*}{L^*},$$
$$u = \frac{u^*}{U^*_\infty},\ v = \frac{1}{\sqrt{Re}}\frac{v^*}{U^*_\infty},\ w = \frac{w^*}{U^*_\infty},$$
$$\omega_x = \frac{1}{Re}\frac{\omega^*_x L^*}{U^*_\infty},\ \omega_y = \frac{\omega^*_y L^*}{U^*_\infty},\ \omega_z = \frac{1}{Re}\frac{\omega^*_z L^*}{U^*_\infty}.$$

Functions a, b and c express nonlinear terms. The curvature influence is represented by d [Floryan and Saric, 1982]. These functions are

$$a = \omega_x(v_b + v) - \omega_y(u_b + u), \tag{5}$$
$$b = \omega_{zb}u + \omega_z(u_b + u) - \omega_x w, \tag{6}$$
$$c = \omega_y w - \omega_{zb}v - \omega_z(v_b + v), \tag{7}$$
$$d = 2u_b u + u^2. \tag{8}$$

Velocity and vorticity components are correlated by

$$\frac{\partial^2 u}{\partial x^2} + \frac{\partial^2 u}{\partial z^2} = -\frac{\partial \omega_y}{\partial z} - \frac{\partial^2 v}{\partial x \partial y}, \tag{9}$$
$$\frac{1}{Re}\frac{\partial^2 v}{\partial x^2} + \frac{\partial^2 v}{\partial y^2} + \frac{1}{Re}\frac{\partial^2 v}{\partial z^2} = -\frac{\partial \omega_z}{\partial x} + \frac{\partial \omega_x}{\partial z}, \tag{10}$$
$$\frac{\partial^2 w}{\partial x^2} + \frac{\partial^2 w}{\partial z^2} = \frac{\partial \omega_y}{\partial x} - \frac{\partial^2 v}{\partial y \partial z}. \tag{11}$$

The continuity equation

$$\frac{\partial u}{\partial x} + \frac{\partial v}{\partial y} + \frac{\partial w}{\partial z} = 0, \tag{12}$$

and convenient boundary conditions close the system for disturbances [Souza et al., 2004, Malatesta et al., 2013].

2.1 The baseflow

The two-dimensional transport equation

$$\frac{\partial \omega_{zb}}{\partial t} + \frac{\partial u_b \omega_{zb}}{\partial x} + \frac{\partial v_b \omega_{zb}}{\partial y} = \frac{1}{Re}\frac{\partial^2 \omega_{zb}}{\partial x^2} + \frac{\partial^2 \omega_{zb}}{\partial y^2}, \tag{13}$$

the continuity equation

$$\frac{\partial u_b}{\partial x} + \frac{\partial v_b}{\partial y} = 0, \tag{14}$$

and the Poisson equation

$$\frac{1}{Re}\frac{\partial^2 v_b}{\partial x^2} + \frac{\partial^2 v_b}{\partial y^2} = -\frac{\partial \omega_{zb}}{\partial x} \tag{15}$$

are considered to represent the boundary layer mean flow.

Our baseflow solution should represent boundary layer flows with pressure gradient distribution different from the neutral case. In this sense we assume the potential flow is represented by

$$U_e = x^m, \tag{16}$$

where m is a local constant associated with the Hartree parameter (γ) by $\gamma = \frac{2m}{m+1}$.

The potential flow velocity and the pressure gradient may be related by the Bernoulli equation

$$U_e \frac{dU_e}{dx} + \frac{dp}{dx} = 0, \tag{17}$$

considering $U_e(x = 1) = 1$.

Baseflow boundary conditions are considered in accordance with Kloker et al. [1993].

3. NUMERICAL METHOD

The geometry of our numerical domain is sketched in Fig. 1. The inflow boundary is represented by $x = x_0$. Flow exits at $x = x_{max}$.

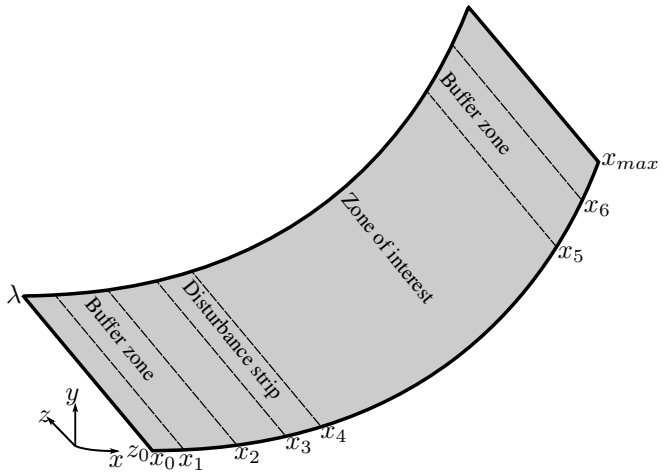

Figure 1. Sketch of our numerical domain. Buffer zones are inserted near inflow and outflow boundaries. A disturbance strip is also shown.

Buffer zones are artificially inserted between points x_1 and x_2 and between x_5 and x_6. These buffer zones are applied in accordance with Kloker et al. [1993]. Disturbances are generated via blowing and suction of mass at the wall in the region between points x_3 and x_4. The steady disturbance amplitude A is here considered to be a real number.

Due to the spanwise quasi-periodic characteristic of the Görtler vortices [Ito, 1980] we can represent the flow quantity $g = \{u, v, w, \omega_x, \omega_y, \omega_z, a, b, c, d\}$ as a linear combination of $K + 1$ Fourier modes

$$g(x, y, z, t) = \sum_{k=0}^{K} g_k(x, y, t) e^{-\iota k \beta z}, \tag{18}$$

where ι is the imaginary unit. Here β represents the spanwise wavenumber

$$\beta = \frac{2\pi}{\lambda}, \tag{19}$$

and λ is the dimensionless wavelength of a pair of vortices.

Equations (2) - (12) are expressed for each Fourier mode k, as

$$\frac{\partial \omega_{xk}}{\partial t} + \frac{\partial a_k}{\partial y} + \iota k \beta b_k - \iota k \beta d_k = \nabla_k^2 \omega_{xk} \tag{20}$$

$$\frac{\partial \omega_{yk}}{\partial t} - \iota k \beta c_k - \frac{\partial a_k}{\partial x} = \nabla_k^2 \omega_{yk} \tag{21}$$

$$\frac{\partial \omega_{zk}}{\partial t} + \frac{\partial b_k}{\partial x} - \frac{\partial c_k}{\partial y} - \frac{\partial d_k}{\partial x} = \nabla_k^2 \omega_{zk} \tag{22}$$

$$\frac{\partial^2 u_k}{\partial x^2} - k^2 \beta^2 u_k = \iota k \beta \omega_{yk} - \frac{\partial^2 v_k}{\partial x \partial y} \tag{23}$$

$$\nabla_k^2 v_k = -\frac{\partial \omega_{zk}}{\partial x} - \iota \beta \omega_{xk} \tag{24}$$

$$\frac{\partial^2 w_k}{\partial x^2} - k^2 \beta^2 w_k = \frac{\partial \omega_{yk}}{\partial x} + \iota k \beta \frac{\partial v_k}{\partial y}, \tag{25}$$

$$\frac{\partial u_k}{\partial x} + \frac{\partial v_k}{\partial y} - \iota k \beta w_k = 0, \tag{26}$$

where $\nabla_k^2 = \left(\frac{1}{Re} \frac{\partial^2}{\partial x^2} + \frac{\partial^2}{\partial y^2} - \frac{1}{Re} k^2 \beta^2 \right)$.

All disturbance calculations are done in the Fourier space but nonlinear products. The streamwise and normal to the wall derivatives are approximated by compact finite difference schemes [Souza et al., 2005]. Spanwise derivatives are calculated straightforward. For a k Fourier mode, Eqs. (20)-(22) are solved by the use of a 4^{th} order Runge-Kutta method.

At each substep of the temporal integrator: (a) the system of linear equations obtained through the discretization of Eq. (24) is solved by a geometric multigrid method [Rogenski et al., 2015]. (b) streamwise and spanwise components of the disturbance velocity are calculated by solving the $1D$ Poisson equations (Eqs. (23) and (25)). (c) vorticity components are updated in the wall. In the last substep of the Runge-Kutta method, vorticity components are filtered by the use of a compact tridiagonal filter [Lele, 1992]. A stationary state is assumed to be reached when the maximum difference between the $k = 1$ spanwise vorticity component is smaller than a given small parameter.

The mean flow state is assumed to be a quasi-$2D$ solution of the Navier-Stokes system of equations. Flow variables are calculated in the physical space. Calculations follow a simplified version of the described disturbance algorithm.

3.1 The boundary conditions

Due to the use of buffer zones close to inflow and outflow boundaries, disturbance values of vorticity and velocity may be consider to be equal to zero. Periodicity is assumed in the spanwise direction. The no-slip and impermeability conditions are assumed for the velocity vector at the rigid boundary but disturbance strip.

At the disturbance generator the v_1 velocity component is imposed to have a $\sin^3$ shape. Vorticity components at the wall are calculated by the use of the expressions

$$\frac{\partial^2 \omega_{x_k}}{\partial x^2} - k^2\beta^2\omega_{x_k} = -\frac{\partial^2 \omega_{y_k}}{\partial x \partial y} - \beta\nabla_k^2 v_k, \tag{27}$$

$$\omega_{y_k} = 0, \tag{28}$$

$$\frac{\partial \omega_{z_k}}{\partial x} = \iota k\beta\omega_{x_k} - \nabla_k^2 v_k. \tag{29}$$

Our numerical domain is chosen to be high enough to ensure vorticity components are equal zero. At the upper boundary the continuity equation is assured and $\frac{\partial v_k}{\partial y} = 0$.

The no-slip and impermeability conditions are also assumed for the baseflow calculations. The vorticity component is calculated considering the two-dimensional

$$\frac{\partial \omega_{z_b}}{\partial x} = -\nabla^2 v_b. \tag{30}$$

At the inflow boundary velocity and vorticity components of the baseflow are assumed to be equal to a Falkner-Skan similar solution. At the upper boundary the meanflow is assumed to be non-rotational. The u_b velocity component is assumed to be represented by a power of the the streamwise position x (see Eq. 16). At the outflow, second derivative of the quantities in the streamwise direction are considered to be zero.

3.2 Secondary instability generation due to unsteady disturbances

Unsteady disturbances are inserted via the same blowing and suction technique that generates the Görtler vortices. The wave package is here defined as the sum of a fundamental frequency (ω_t) sine function and its higher harmonics and it is represented by

$$v_1(x, 0, t) = A_s\, q(x) \sum_{m=1}^{M} sin\left(\frac{m\omega_t t}{2\pi}\right), \tag{31}$$

where $q(x)$ is a 8^o polynomial function with maximum equals one and extrema equal zero and M denotes the maximum number of harmonics. The constant A_s is a complex number that selects the preferable secondary instability mechanism [Souza, 2003]. Here, if A_s is a real number the flow may transition via the amplification of the varicose mode. A sketch of this configuration is illustrated by Fig. 2(a). Otherwise, if A_s is a purely imaginary number the flow may transition due to the growth of the sinuous mode (see Fig. 2(b)).

4. RESULTS

Nonlinear simulations are carried out considering the same physical parameters of the classical experiments of Swearingen and Blackwelder [1987]. We consider the radius of the concave surface $R^* = 3.2\ m$. For all simulations the external velocity is $U_\infty^* = 5.0\ m.s^{-1}$ in $L^* = 0.1\ m$. Kinematic viscosity is $\nu^* = 1.5 \times 10^{-5}\ m^2.s^{-1}$.

The Reynolds and Görtler numbers are defined in a streamwise position L^*. We assume

$$Re = \frac{U_\infty^* L^*}{\nu^*} \text{ and } Go = Re^{\frac{1}{4}}\sqrt{\frac{L^*}{R^*}}. \tag{32}$$

The spanwise wavelength of the vortices is defined in terms of the characteristic wavelength parameter

$$\Lambda = \frac{U_\infty^* \lambda^*}{\nu^*}\sqrt{\frac{\lambda^*}{R^*}}. \tag{33}$$

Figure 2. Diagram of unsteady disturbances generation in a primary instability flow. Extrated from Souza [2011]

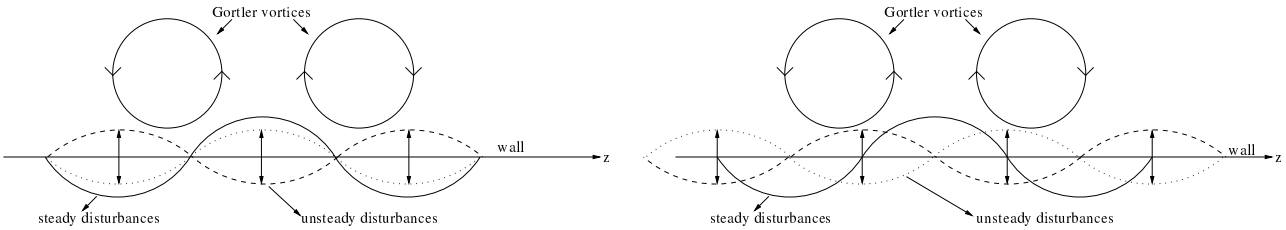

(a) in phase

(b) out of phase in 90^o

The $\Lambda = 450$ describes the characteristic size of the vortices. For this case, three different external pressure gradient configurations are investigated: a favourable case $dp/dx = -0.02$, an adverse case $dp/dx = 0.008$ and the neutral case $dp/dx = 0.0$. The external streamwise velocity U_e and shape factor H_{12} for the three cases are presented by Fig. 3.

Figure 3. Baseflow characteristics for three different external pressure distributions.

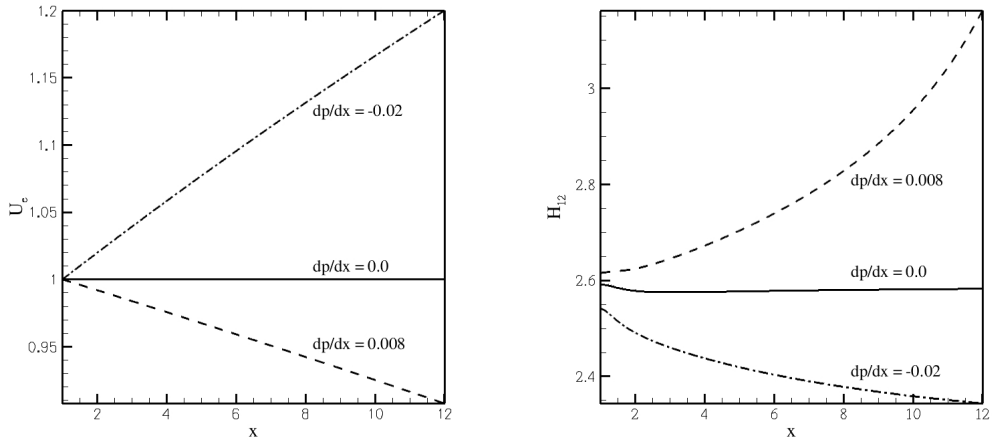

(a) external streamwise velocity U_e

(b) shape factor H_{12}

Different sets of numerical parameters have been tests and the following results are considered to be grid-independent. The numerical code and model have been verified and validated through Linear Stability Theory, numerical, and experimental literature results.

Simulations adopt 21 Fourier modes with 64 collocated points in the physical space. For each Fourier mode a $2D$ y-stretched mesh is generated. We consider 2201 points in the x-direction with step size $dx = 5.0 \times 10^{-3}$. In the y-direction 225 points with first step size $dy = 8.0 \times 10^{-2}$ and stretching factor $sf = 1\%$ are used. The time step is 2.5×10^{-3}. Buffer zones and the disturbance region are defined close to the boundaries as $[x_0;\ x_1;\ \ldots;\ x_{max}] = [1;\ 1;\ 1.28;\ 1.48;\ 1.88;\ 11;\ 11.75;\ 12]$. Three different wave packages are inserted in a region near the primary flow saturation region. Each package has a streamwise length of 0.25, $\omega_t = 20\ Hz$ as the fundamental frequency and fifteen harmonics. The temporal Fourier analysis follows metrics provided by Wassermann and Kloker [2002]. Here it is considered 64 samples in a period for the Fourier analysis.

Initially we are going to describe the evolution of the sinuous and varicose modes for the neutral pressure gradient configuration. Following Souza [2011], the sinuous mode is obtained by taking $A_s = 0 + 1.5 \times 10^{-2}\ \iota$. In the same way, the in phase case considers $A_s = 1.5 \times 10^{-2} + 0\ \iota$. For both cases, the wave packages are inserted in positions $[5.4, 5.65]$, $[5.9, 6.15]$ and $[6.4, 6.65]$. In Fig. 4(a) the maximum amplitude of each frequency $m = 1, ..., 16$ is presented for the sinuous case. In phase results are presented in Fig. 4(b). Following Wassermann and Kloker [2002] the temporal Fourier analyses consider both the streamwise velocity and the second derivative of the streamwise velocity. The interruption presented in both figures presents changes in the analyzed function. In the left we analyze the temporal evolution of the second derivative of u. In the right, the temporal analysis considers the u velocity.

Based on Fig. 4 one may observe that there are interactions between the temporal disturbance packages and the

Figure 4. Evolution of unsteady disturbances on the Görtler flow with $dp/dx = 0.0$. In (a) unsteady disturbances are out of phase and in (b) unsteady disturbances are in phase with the primary flow.

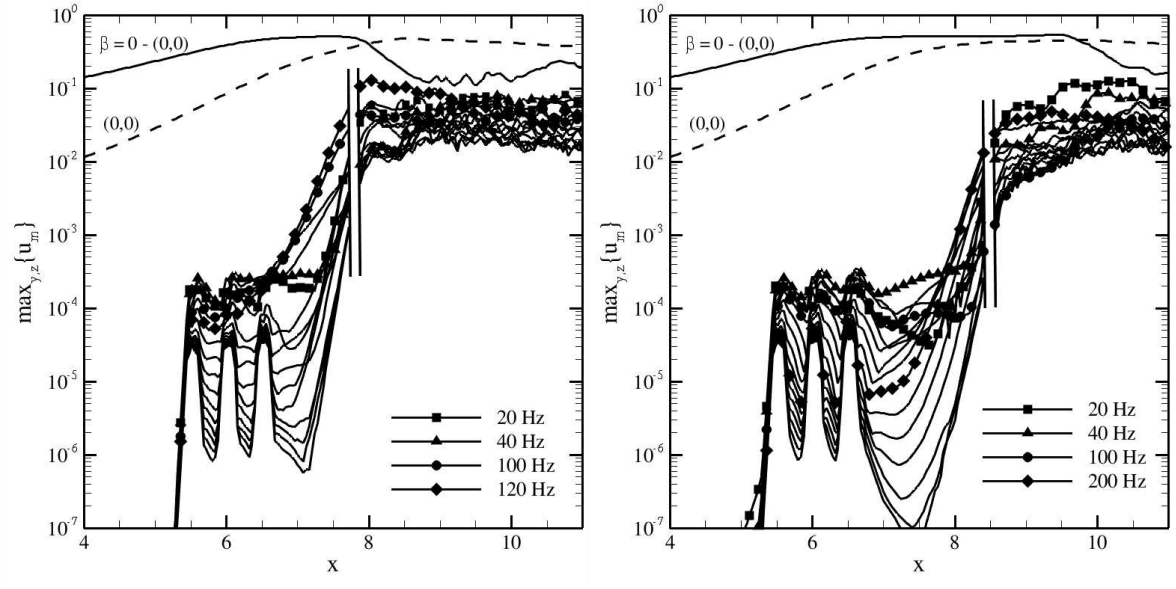

(a) (b)

primary flow for both cases. In the region close to the unsteady disturbance strips, a low frequency mode grows slower than a high frequency one. It implies that the flow transition from a primary state to a secondary state is likely to occur through the amplification of higher frequencies. High frequencies grow closer to the leading edge for the sinuous mode. They start to grow exponentially at $x \geq 6.5$ in (a) and $x \geq 7.5$ in (b). In this way one may assume the sinuous mode is more unstable than the varicose one at least for the present configuration.

The influence of a favourable pressure gradient regime is investigated and the temporal Fourier analysis for the sinuous and varicose modes is presented in Fig. 5. For the favourable case $(dp/dx = -0.02)$, the wave packages are inserted in positions $[5.95, 6.2]$, $[6.45, 6.7]$ and $[6.95, 7.2]$. In Fig. 6 the evolution of the Fourier modes represents the behaviour of the secondary instability for the adverse regime $(dp/dx = 0.008)$.

A similar behaviour can be observed in Fig. 5 for the favourable cases. The sinuous mode shows to be more unstable than the varicose one. Exponential growth is observed in $x \geq 7$ for the (a) case and $x \geq 8$ for the (b) case.

The adverse pressure gradient case shows to be the most unstable case. The exponential growth of the sinuous mode occurs in $x \geq 6$ and in $x \geq 6.5$ for the varicose mode.

It is also important to identify which mode would dominate the transition in the case of competition between the sinuous and varicose modes. Based on earlier results, it is reasonable to predict that the sinuous mode dominates the transition. Aimed to verify this state, the competition between both secondary modes is imposed by considering $A_s = 0.75\sqrt{2} \times 10^{-2}(1.0 + 1.0\,\imath)$. In Fig. 7 the temporal analysis for the adverse, neutral and favourable cases are presented in (a), (b) and (c), respectively.

Fig. 7 reaffirms the adverse case as the most unstable one. The sinuous behaviour of the instability can be visualized by the use of Q-criterion with $Q = 0.5$ and is illustrated by Fig. 8 for the three cases.

The evolution of the temporal modes are similar to the purely sinuous cases provided by Figs. 4-6.

5. CONCLUSIONS

Both the sinuous and varicose modes are considered to be potentially responsible for transition in boundary layers over concave surfaces for cases where the pressure gradient is different from zero. We observe that the favourable and neutral pressure gradient cases are more stable than the adverse one. For all the cases described here the sinuous mode shows to be the most unstable mode.

Figure 5. Evolution of unsteady disturbances on the Görtler flow with $dp/dx = -0.02$. In (a) unsteady disturbances are out of phase and in (b) unsteady disturbances are in phase with the primary flow.

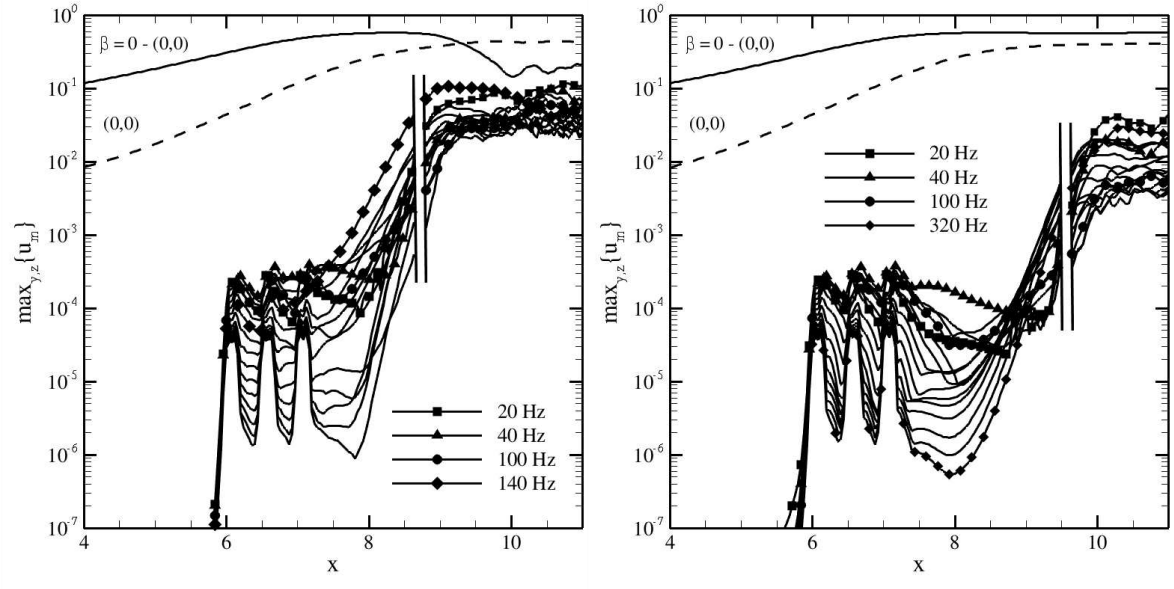

(a) (b)

Figure 6. Evolution of unsteady disturbances on the Görtler flow with $dp/dx = 0.008$. In (a) unsteady disturbances are out of phase and in (b) unsteady disturbances are in phase with the primary flow.

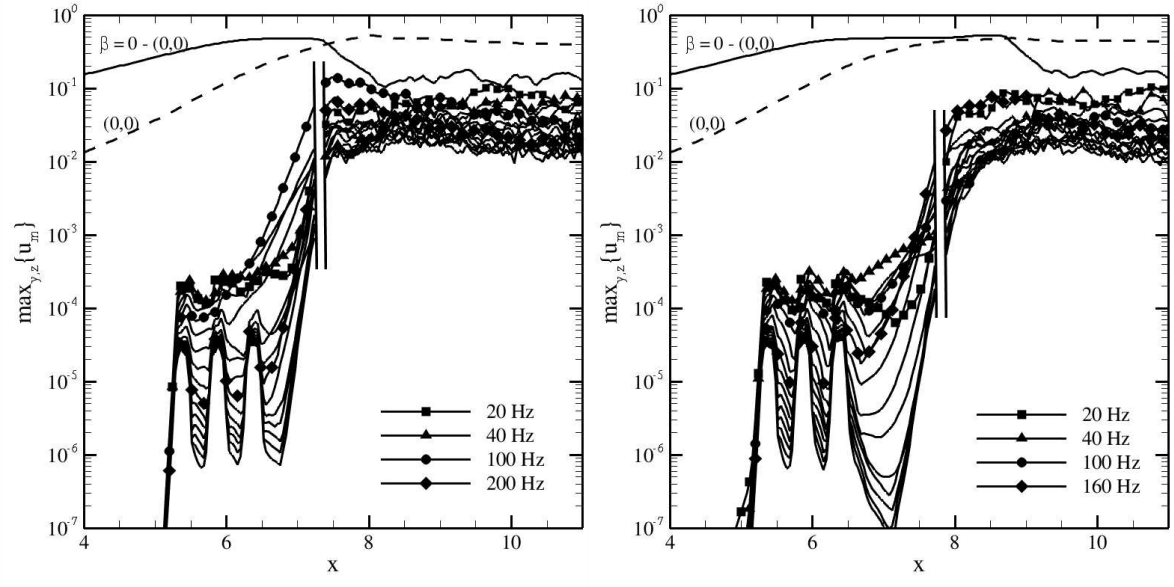

(a) (b)

6. ACKNOWLEDGEMENTS

The authors acknowledge Professors M T de Mendonça, J M Floryan and M J Kloker for fruitful discussions. Josuel acknowledges the São Paulo Research Foundation(FAPESP) for financial support under grant #2011/08010-0 and the National Council for Scientific and Technological Development(CNPq) under grant #401032/2014-0. We also thank CEPID-CeMEAI for computational time.

Figure 7. Competition between the even and odd modes in cases where (a) $dp/dx = 0.008$, (b) $dp/dx = 0.0$ e (c) $dp/dx = -0.02$

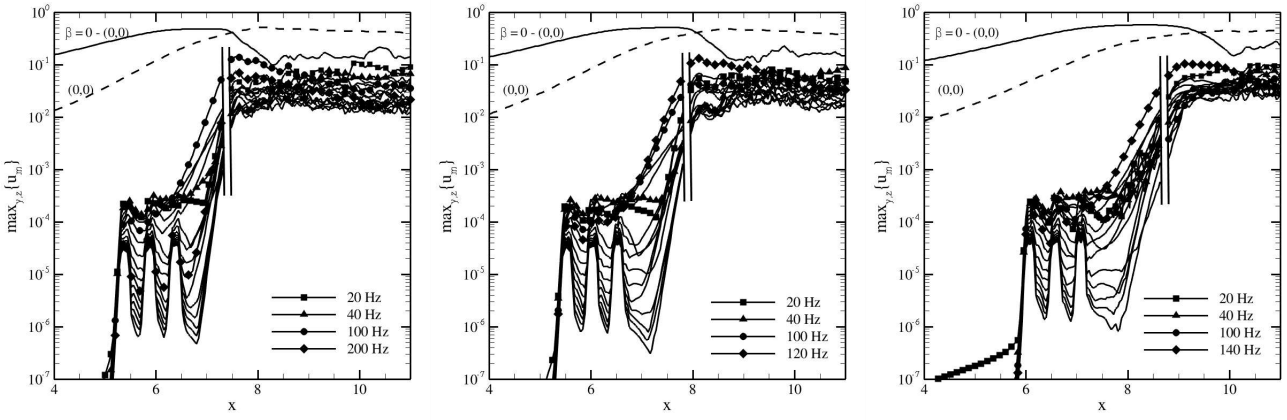

(a) (b) (c)

Figure 8. Visualization of vortical secondary structures by the use of Q-criterion in cases where both sinuous and varicose modes compete. In (a) $dp/dx = 0.008$, (b) $dp/dx = 0.0$ and (c) $dp/dx = -0.02$.

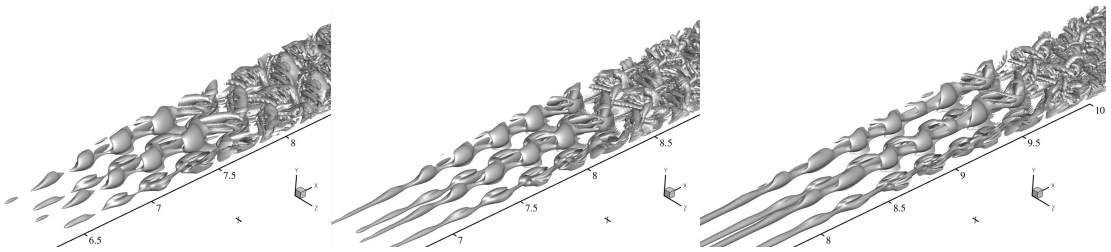

(a) (b) (c)

7. REFERENCES

Y. Aihara and T. Sonoda. Effects of pressure gradient on the secondary instability of Görtler vortices. In *AIAA 19th Aerospace Sciences Meeting*, 1981.

F. Bahri, Y. Koyama, J. Iino, and Aota. Effect of the pressure gradients on the secondary instability of Görtler flow. In *IUTAM Symposium on Laminar-turbulent transition*, 1999.

J. M. Floryan and W. S. Saric. Stability of Görtler vortices in boundary layers. *AIAA Journal*, 20(3):316–324, 1982.

P. Hall and N. J. Horseman. The linear inviscid secondary instability of longitudinal vortex structures in boundary layers. *J. Fluid Mech.*, 232:357–375, 1991.

A. Ito. The generation and breakdown of longitudinal vortices along a concave wall. *J. Japan Soc. Aero. Space Sci.*, 28: 327–333, 1980.

M. Kloker, U. Konzelmann, and H. F. Fasel. Outflow boundary conditions for spatial Navier-Stokes simulations in transition boundary layers. *AIAA Journal*, 31(4):620–628, 1993.

S. Lele. Compact finite difference schemes with spectral-like resolution. *Journal of Computational Physics*, 103:16–42, 1992.

F. Li and M. R. Malik. Fundamental and subharmonic secondary instability of Görtler vortices. *J. Fluid Mech.*, 297: 77–100, 1995.

V. Malatesta, L. F. Souza, and J. T. C. Liu. Influence of Goertler vortices spanwise wavelenght on heat transfer rates. *Computation Thermal Sciences: An International Journal*, 5(5):389–400, 2013.

H. Mitsudharmadi, S. H. Winoto, and D. A. Shah. Splitting and merging of Görtler vortices. *Physics of Fluids*, 17:1–12, 2005.

H. Mitsudharmadi, S. H. Winoto, and D. A. Shah. Development of most amplified wavelength Görtler. *Physics of Fluids*, 18:1–12, 2006.

J. K. J. K. Rogenski, L. A. Petri, and L. F. Souza. Effects of parallel strategies in the transitional flow investigation. *J. Braz. Soc. Mech. Sci. Eng.*, 37:861–872, 2015.

W. S. Saric. Görtler vortices. *Annual Review of Fluid Mechanics*, 26:379–409, 1994.

Lars-uve Schrader, Luca Brandt, and Tamer A. Zaki. Receptivity, instability and breakdown of Görtler flow. *J. Fluid Mech.*, 682:362–396, 2011.

L. F. Souza. Estudo numérico de instabilidade secundária em escoamentos de goertler. Livre docência, Universidade de São Paulo, 2011.

L. F. Souza, M. T. Mendonça, M. A. F. de Medeiros, and M. Kloker. Seeding of Görtler vortices through a suction and blowing strip. *Journal of the Brazilian Society of Mechanical Sciences*, XXVI:269–279, 2004.

L. F. Souza, M. T. Mendonça, and M. A. F. Medeiros. The advantages of using high-order finite differences schemes in laminar-turbulent transition studies. *International Journal for Numerical Methods in Fluids*, 48:565–592, 2005.

Leandro F. Souza. *Instabilidade centrífuga e transição para turbulência em escoamentos laminares sobre superfícies côncavas*. PhD thesis, Instituto tecnológico de aeronáutica, 2003.

J. D. Swearingen and R. F. Blackwelder. The growth and breakdown of streamwise vortices in the presence of a wall. *Journal of Fluid Mechanics*, 182:255–290, 1987.

Tandiono, S. H. Winoto, and D. A. Shah. Visualizing shear stress in Görtler vortex flow. *Journal of Visualization*, 12(3): 195–202, 2009a.

Tandiono, S. H. Winoto, and D. A. Shah. Wall shear stress in Görtler vortex boundary layer flow. *Physics of Fluids*, 21: 1–9, 2009b.

Peter Wassermann and Markus Kloker. Mechanisms and passive control of crossflow-vortex-induced transition in a three-dimensional boundary layer. *J. Fluid Mech.*, 456:49–84, 2002.

S. H. Winoto, H. Mitsudharmadi, and D. A. Shah. Visualizing Görtler vortices. *Journal of Visualization*, 8(4):315–322, 2005.

8. RESPONSIBILITY NOTICE

The authors are the only responsible for the printed material included in this paper.